Controlling solvent quality by time: Self-avoiding sprints in nonequilibrium polymerization

Michael Bley[1,*] Upayan Baul[1] and Joachim Dzubiella[1,2,†]

[1]*Applied Theoretical Physics–Computational Physics, Physikalisches Institut, Albert-Ludwigs-Universität Freiburg, D-79104 Freiburg, Germany*

[2]*Cluster of Excellence livMats@FIT–Freiburg Center for Interactive Materials and Bioinspired Technologies, Albert-Ludwigs-Universität Freiburg, D-79110 Freiburg, Germany*

(Received 29 June 2021; accepted 22 August 2021; published 16 September 2021)

A fundamental paradigm in polymer physics is that macromolecular conformations in equilibrium can be described by universal scaling laws, being key for structure, dynamics, and function of soft (biological) matter and in the materials sciences. Here we reveal that during diffusion-influenced, *nonequilibrium* chain-growth polymerization, scaling laws change qualitatively, in particular, the growing polymers exhibit a surprising self-avoiding walk behavior in poor and θ solvents. Our analysis, based on monomer-resolved, off-lattice reaction-diffusion computer simulations, demonstrates that this phenomenon is a result of (i) nonequilibrium monomer density depletion correlations around the active polymerization site, leading to a locally directed and self-avoiding growth, in conjunction with (ii) chain (Rouse) relaxation times larger than the competing polymerization reaction time. These intrinsic nonequilibrium mechanisms are facilitated by fast and persistent reaction-driven diffusion ("sprints") of the active site, with analogies to pseudochemotactic active Brownian particles. Our findings have implications for time-controlled structure formation in polymer processing, as in, e.g., reactive self-assembly, photocrosslinking, and three-dimensional printing.

DOI: 10.1103/PhysRevE.104.034501

I. INTRODUCTION

Polymer physics provides universal scaling concepts [1–5] which have strongly shaped the research in the natural and life sciences as well as engineering over the past decades [6–12]. Paradigmatic are simple scaling concepts in equilibrium, e.g., for the end-to-end distance of a chainlike polymer, $R_{ee} \propto N^{\nu}$, where the conformational scaling exponent ν depends on the solvent quality. For a purely random walk (ideal or θ solvent), $\nu \simeq 1/2$, while for poor solvents the polymer collapses and $1/3 < \nu \lesssim 1/2$, and for athermal solvents $\nu \simeq 3/5$, constituting the well-known self-avoiding walk (SAW) or "Flory" scaling [1] for swollen conformations. Most polymers exhibit a universal scaling behavior of various structural and dynamic properties, such as coil dimensions and relaxation, despite a different chemical composition. This universality (in equilibrium) across length and timescales formed the basis for the extraordinary historical success of polymer physics in a wide range of fields.

However, functional materials are typically synthesized, processed, and functioning under *nonequilibrium* conditions. Hence, growing attention has been drawn to investigate nonequilibrium polymer properties, how to conserve and control them, and their consequences on material design. In particular, the possibility of generating stored, "extra" free energy, stresses, and memory emerges, which can be potentially harvested for the design of highly responsive, interactive, or even adaptive materials [13–16]. The anticipated wide range of new structural, dynamical, and mechanical properties arises from the nonequilibrium competition between the timescales of (reaction) synthesis, processing, polymer relaxation, and observation (function) [17–24]. However, such a complex competition of timescales, often also involving spatial modulation and spatiotemporal correlations, has hampered our understanding of nonequilibrium polymer properties up to date.

For synthesizing strongly "out-of-equilibrium polymers," the type of kinetics and in particular the speed of the polymerization reaction play a key role. Most of the common and commercially used polymer architectures are produced by chain polymerization techniques [1,25] such as radical polymerization. Controlling (fast) photopolymerization reactions is crucial for mastering high-resolution three-dimensional (3D) and 4D printing techniques [12,26,27]. Polymerization is also possible on colloidal scales by guided, diffusion-controlled self-assembly of supracolloidal polymer chains [28,29]. However, structural insights are sparse and quantitative kinetic rate laws still absent. Importantly, experiments observe large macroscopic changes during and after synthesis, e.g., retarded material shrinkages associated with the fast polymerization during the autoacceleration phase [30] (also Trommsdorff-Norrish or gel effect [31,32]), whose microscopic mechanisms remain unexplained.

On the fundamental level, magnetic-tweezer experiments of the real-time dynamics of a growing polymer indeed demonstrated a competition between reaction and conformational relaxation times [33]. Studies on chain walking catalysis of dendritic polymers [34] also reported a

*michael.bley@physik.uni-freiburg.de
†joachim.dzubiella@physik.uni-freiburg.de

dependence of the emerging structure on the reaction rate: High rates lead to linear structures, while lower ones formed hyperbranched structures, hinting to a nonequilibrium conformational behavior tunable by the rate. While molecular computer simulations of growing polymer chains have been performed [35–39], they either *a priori* assumed good solvent conditions in their models or did not systematically investigate nonequilibrium behavior in varying solvent qualities. However, classical theoretical concepts for diffusion-influenced polymerization kinetics [17,31,32,40] shall strongly benefit from studies with a spatiotemporal, particle-level resolution including memory or proximity effects.

In particular, lattice models such as the growing-SAW (GSAW) have been applied to study the polymer growth in a good solvent by means of a weighted choice of the next bond formation [41,42], and which have been used by Taniya *et al.* [43] in combination with Monte Carlo simulations to study conformational differences in nonequilibrium polymerization. Due to the *a priori* definition of weighted growth probabilities, the GSAW approach already implies good solvent conditions and a SAW behavior. No localized monomer-depletion around the growing end as well as heterogeneous (in time and space) chain relaxation effect are considered there, in contrast to the present work.

Here, using off-lattice, monomer-resolved reaction-diffusion computer simulations of chain-growth polymerization of a single polymer, we demonstrate that solvent quality can be controlled by timescales in nonequilibrium and also depends on the time of of observation. In other words, we observe substantial nonequilibrium effects on the conformational properties of the growing chain: For fast polymerization, the time-dependent size of the polymer exhibits an unexpected SAW scaling in ideal and θ-solvent conditions, and also enhanced scaling exponents in poor solvents, before they relax back into equilibrium. Our surprising findings can be explained by intrinsic nonequilibrium spatiotemporal correlations leading to local structural depletion and directed growth of monomers, related to pseudochemotactic active Brownian particles (ABPs) [44] steered by nutrition concentration gradients [45,46]. The key for understanding is the competition of the various important timescales (diffusion, reaction, chain relaxation, observation) in the system, realizable only in a certain parameter window of intrinsic reaction propensities and monomer densities, which we discuss in detail. Our results will be useful for various materials applications where structure formation in nonequilibrium synthesis and processing can be controlled by time.

II. REACTION RATES OF GROWING CHAINS

A. Macroscopic rate laws

In our reactive Brownian dynamics simulation framework, the chain polymerization propagates as

$$P_{N-1} - AC + M \xrightarrow{k(\lambda)} P_N - AC, \tag{1}$$

where $P_{N-1} - AC$ is a polymer chain consisting of $N-1$ nonreactive monomers and with a terminal active center (AC), which reacts with a free monomer M in the surrounding solution with monomer density $\rho(t)$ irreversibly with a reaction rate constant $k(\lambda)$ to form a chain with one additional bonded monomer $P_N - AC$. Figure 1(a) illustrates a propagation step: If free monomers are found within the reactive volume of the AC, then a new bond is formed between the AC and the closest free monomer with a reaction frequency or "propensity" λ. The latter interpolates between reaction-control and diffusion-control [32,47]. The quality of the (implicit) solvent in our simulations is tuned by the interaction parameter ε in the Lennard-Jones interaction between the monomers: $\varepsilon = 0$ is a perfectly ideal chain and ε_θ describes real-chain θ conditions, such that $\varepsilon < \varepsilon_\theta$ are good solvent conditions and $\varepsilon > \varepsilon_\theta$ are poor solvent conditions in equilibrium (see Appendix A).

Typically such reaction kinetics would be described as pseudo–first order [48], since the concentration of the AC, $\rho_{\mathrm{ac}} = V^{-1}$, remains constant in the total volume V. The concentration of free monomers is initially $\rho_0 = \rho(t=0) = N_{m,0}/V$ with $N_{m,0}$ as the initial monomer concentration. The elementary rate law and its integrated form for the time-dependent concentration $\rho(t)$ of free momomers then is written as follows:

$$\frac{d\rho(t)}{dt} = -k(\lambda)\rho(t)\,\rho_{\mathrm{ac}} \quad \text{and} \quad \rho(t) = \rho_0 e^{-tk(\lambda)\rho_{\mathrm{ac}}}, \tag{2}$$

where the degree of polymerization is $N(t) = -V d\rho(t)/dt$. This simple first-order kinetics says that the concentration of monomers should decay exponentially with a timescale set by $V/k(\lambda)$ and the polymer grows with a timescale (inverse rate) $\tau_{\mathrm{react}} = [k(\lambda)\rho(t)]^{-1}$.

Reactions are fast (i.e., diffusion-influenced or controlled) if the propensity λ is large and/or the free monomer density ρ is large. Simulation results for the polymerization are exemplified in Fig. 1(b) for three selected reaction propensities λ and initial monomer bulk density $\rho_0\sigma^3 = 0.3$, (σ is the size of a monomer and sets our length scale). The snapshots taken from growing chains at high and low λ [red and blue in Fig. 1(c)] already indicate that they exhibit differences in the topological growth behavior: A fast growth leads to more extended chains, whereas slower reaction propensities yield a more compact, sometimes even globular chain structure. Importantly, in Fig. 1(b) we find that the elementary law (2), fitted to the data for initial times cannot quantitatively describe the overall polymerization rate for the faster reactions, that is, at the higher propensities clear deviations are observed for increasing polymerization time.

B. Microscopic description of reaction rate coefficients

One dominant reason for the failure of first-order kinetics is the coupling between the reaction itself and a reaction-driven jump-diffusion of the active end-monomer [32,40], which was introduced already in the seminal work by Schulz [31] as "reaction-diffusion" and verified experimentally [49]. Theories for diffusion-influenced bimolecular reactions require these diffusion coefficients, e.g., as in the here relevant Doi scheme [47,50],

$$k(\lambda) = 4\pi DR\left[1 - \frac{\tanh\left(R\sqrt{\frac{\lambda}{D}}\right)}{R\sqrt{\frac{\lambda}{D}}}\right], \tag{3}$$

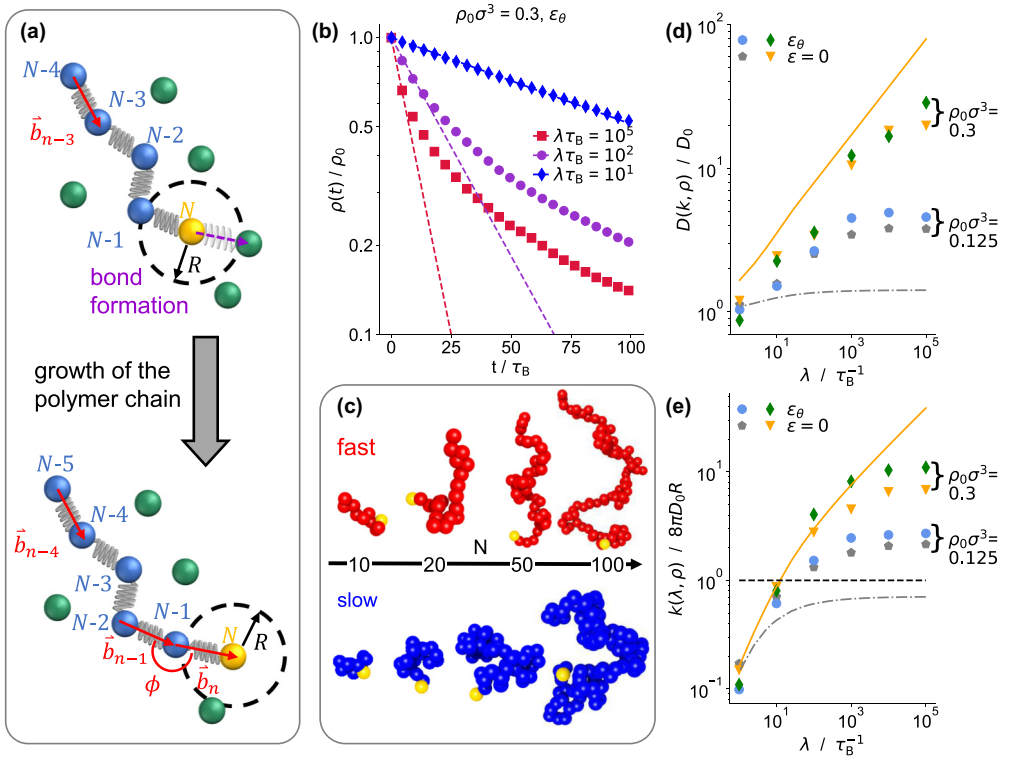

FIG. 1. Simulation and kinetics of a growing polymer chain. (a) Schematic representation of the growth step of a polymer chain (blue) with an active center (AC, yellow) with reactive radius R and reaction propensity λ. During a reaction a bond is formed between a free monomer of size σ (green) and the AC to propagate the chain. The newly added monomer spans up an angle ϕ by the terminal two bond vectors $\vec{b}_{n-1}$ and $\vec{b}_n$ during bond formation. The newly attached monomer becomes the new active center. (b) Concentration of free monomers $\rho(t)/\rho_0$ scaled by its initial value $\rho_0\sigma^3 = 0.3$ for fast (red; $\lambda = 10^5\ \tau_B^{-1}$), intermediate (magenta;$10^2\ \tau_B^{-1}$), and slow (blue; $\lambda = 10^1\ \tau_B^{-1}$) reactions versus time t (scaled by the Brownian timescale $\tau_B = \sigma^2/D_0$) at θ conditions, $\varepsilon = \varepsilon_\theta$. Symbols represent simulated data, the lines show the corresponding fits to initial times according to the first order rate equation (2). (c) Snapshots of fast (red) and slowly (blue) growing chains. (d) Total diffusion coefficient $D(\lambda, \rho)$ versus reaction propensity λ for perfectly ideal ($\varepsilon = 0$) and real chain θ conditions, $\varepsilon = \varepsilon_\theta$ (simulation: symbols; dash-dotted gray and orange line: Numerical solutions from the set of coupled Eqs. (3) and (4) for $D_{\rm tb} = D_m/N$ with $\alpha = 1.0$ and $D_{\rm tb} = D_m$ with $\alpha = 1.41$, respectively). (e) Scaled reaction rate $k(\lambda, \rho)$ for the same parameters [simulation: Symbols; dash-dotted gray and orange line: Numerical solutions from the set of coupled Eqs. (3) and (4) for $D_{\rm tb} = D_m/N$ with $\alpha = 1.0$ and $D_{\rm tb} = D_m$ with $\alpha = 1.41$, respectively]; horizontal dashed black line: Smoluchowski bimolecular reaction rate $k_S = 8\pi D_0 R$.

where $R = \sqrt[6]{2}\sigma$ represents the reaction radius around the active center. The Doi rate approaches the classical Smoluchowski rate [32,47] for complete diffusion control, $k = 4\pi DR$, for infinitely fast propensities, $\lambda \to \infty$.

C. Coupling between active center diffusion and reaction rates

The mutual diffusion coefficient D between particles A and B is $D = D_A + D_B$. In the case of a growing polymer chain, thus [32]

$$D(k, \rho) = D_m + D_{\rm ac}(k, \rho) = D_m + D_{\rm tb} + D_{\rm jump}(k, \rho), \quad (4)$$

consisting of the contribution by the free monomers D_m and the reaction-rate-dependent diffusion of the chain's active center $D_{\rm ac}(k, \rho)$. The latter is the sum of the thermal, fluctuation-induced diffusion of the terminal bead $D_{\rm tb}$ and a jump (reaction-)diffusion $D_{\rm jump}(k, \rho)$. $D_{\rm tb}$ depends on the relaxation timescales of a polymer chain consisting of N monomers, which are described by the Rouse model [4,5,51]: A chain segment of length $N/p =: s$ relaxes with a timescale $\tau_p \approx b^2/(6\pi^2 D_m)s^2$. The Rouse time $\tau_{\rm Rouse}$ is the (longest) relaxation time of the whole chain ($s = N$), while $\tau_m \approx b^2/(6\pi^2 D_m)$ represents the Kuhn monomer relaxation time for the highest mode, $s = 1$. Let us compare the reaction timescales $\tau_{\rm react} = (k\rho)^{-1}$ with τ_m and $\tau_{\rm Rouse}$. For short times $\tau_{\rm react} \lesssim \tau_m$, the fastest diffusive behavior with $D_{\rm tb} \simeq D_m$ should apply. At long reaction timescales ($\tau_{\rm react} \gg \tau_{\rm Rouse}$), the slowest diffusive behavior following the chain center-of-mass with $D_{\rm tb} \simeq D_m/N$ is recovered [5,51]. It should be noted that for intermediate reaction timescales $\tau_m > \tau_{\rm react} > \tau_{\rm Rouse}$ subdiffusive behavior for the AC is reported [5], which corresponds to a diffusion coefficient $D_{\rm tb} = D_m(\tau_m/\tau_{\rm react})^{1/2}$. Hence, depending on the reaction timescale, different diffusion scales are relevant for the AC motion and the growth process.

The second contribution, $D_{\rm jump}(k, \rho) = \alpha b^2 \rho k(\lambda)/6$, covers a "jump" process, since after the formation of a new bond in the chain, the AC moves discretely by one bond length b to be the new terminal chain element. This maps to diffusive, random-walk behavior in 3D with step length b and jump rate $\rho k(\lambda)$ [17,31,32,40]. Importantly, the jump diffusion is determined by the reaction rate itself, thus requiring a self-consistent solution of Eqs. (3) and (4), which we explicitly perform below. Moreover, in this work we uncover that fast

growth leads to a locally directed, less random motion of the AC. We consider this effect by introducing the coefficient $\alpha = \tau_{\rm rot}/\tau_{\rm react} = \tau_{\rm rot}\rho k(\lambda)$. The rotational reorientation time $\tau_{\rm rot}$ describes in analogy to active Brownian particles (ABPs) [44] the direction memory, or persistence, of translational motion. Here the lower limit $\alpha = 1.0$, where $\tau_{\rm rot} = \tau_{\rm react}$ (that is, completely random attachment of a new monomer) represents no persistence, while $\alpha > 1.0$ and thus $\tau_{\rm rot} > \tau_{\rm react}$ covers a directed growth behavior. The latter leads to enhanced long-time diffusion as for ABPs [44], since between multiple growth events the chain does not loose its directional memory.

These considerations lead to lower and upper limits for the mutual diffusion $D(\lambda, \rho)$ and the rate $k(\lambda)$ to describe our simulation data. The slow limit is obtained by assuming the longest Rouse relaxation and $\alpha = 1$, involving no fit parameter. The fast limit assumes the fastest, short-time diffusion for the terminal bead and uses α as a fit parameter to describe our fastest data. For $\rho_0\sigma^3 = 0.3$, a value of $\alpha = 1.41$ is found. Figure 1(d) displays the mutual diffusion constant $D(\lambda, \rho_0)$ from simulations (symbols) compared with the self-consistent numerical solution of Eqs. (3) and (4) for the fast and slow diffusion limits, where we used $\rho = \rho_0$ for simplicity in our qualitative discussion. In Fig. 1(e) we show a comparison of the corresponding rates. Note that the simulated rate can be one order of magnitude faster than the classical Smoluchowski limit, because the jump diffusion leads to fast "sprints" of the AC. The figure thus shows that for propensities $\lambda > 10\,\tau_B^{-1}$, not only the diffusion contribution of the terminal bead $D_{\rm tb}$, but also the inclusion of $D_{\rm jump}$ is required to describe the simulated reaction rate coefficients (symbols). Our analysis demonstrates that our improved diffusion rate theory serves as a very reasonable orientation for the accessible range of diffusion coefficients for growing polymer chains, while quantitative rate descriptions are still very challenging due to the complex competition of timescales, and because of nonequilibrium structural effects as we will explore deeper below.

We note that in the diffusion-controlled (dc) limit $\lambda \to \infty$ (and assuming $\alpha = 1$ for simplicity), we derived an analytical expression for the total (self-consistent) rate, yielding

$$k_{\rm dc}(\rho) = \frac{4\pi\,(D_m + D_{\rm tb})R}{1 - \frac{2}{3}\pi R b^2 \rho}. \tag{5}$$

The result is remarkable for two reasons: (i) during the reaction $\rho(t)$ decreases and the rate slows down beyond first order kinetics, which explains our observations in Fig. 1(b). And (ii) the denominator of Eq. (5) diverges at a critical monomer density of $\rho_{\rm crit} = (2/3\pi R b^2)^{-1} \approx 0.43\ \sigma^{-3}$. The physics behind this behavior is that for higher densities of the free monomers, the jump diffusion of the active center becomes so fast that after every jump a new reacting monomer will be found with high probability. Very fast cascade reactions (very fast "sprints") become possible where segments grow almost instantaneously and the rate diverges. The critical density $\rho_{\rm crit}$ can thus be viewed as a dynamical percolation threshold for fast growth reactions. We indeed observe indications of such a cascading behavior for fast reactions at higher densities as discussed further below. In radical polymerization of dense, many-chain systems with hindered termination this is probably related to the autoacceleration which can lead to a polymerization "explosion" [30,32].

III. EMERGING PROPERTIES FROM SIMULATED CHAIN GROWTH

A. Polymer size scaling for different reaction rates

The fast propagation of the chain leads to unexpected structural and conformational effects, in particular for how the polymer size changes with the degree of polymerization N ("size scaling"). Figures 2(a) and 2(b) show end-to-end distances $R_{\rm ee}(N)$ of growing chains at densities $\rho_0 = 0.125$ and $0.3\ \sigma^{-3}$, respectively, in ideal and θ-solvent conditions. The simulated data has been fitted with the typical power law $R_{\rm ee} = bN^{\nu}$ to obtain the scaling exponents ν. In stark contrast to the equilibrium case, nonequilibrium growing chains in fast reaction conditions ($\lambda = 10^5$) yield size scaling exponents representing a SAW scaling, that is, $\nu \simeq 3/5$. For lower propensities ($\lambda = 10^0$), equilibrium scaling, $\nu \simeq 1/2$, is recovered. The end-to-end distances $R_{\rm ee}(N)$ are calculated in our simulations immediately after the formation of a new bond, and for each $N(t)$ all $R_{\rm ee}$ of a system are averaged. These averaged $R_{\rm ee}[N(t)]$ are functions of time t and thus the underlying chain conformations contain the information from the nonequilibrium processing in comparison to the relaxed equilibrium counterpart.

The dependence of ν with propensity λ for the two densities is summarized in Fig. 2(c): Clearly, low propensities λ yield smaller exponents $\nu(\lambda, \rho_0)$, and for both cases (fully noninteracting and ε_θ) the random-walk value of $1/2$ is fully recovered. For larger propensites, $\lambda \gtrsim 10^2$, a transition to SAW scaling is observed for both ideal and θ conditions and both densities. Note that the scaling exponent is lower for the higher density, $\rho_0\sigma^3 = 0.3$, although the total propagation rate is higher. This trend must be assigned to the existence of the dynamic percolation limit as predicted by equation (5), which is approached here. Hence, the scaling exponents are depending nonmonotonically on density. We will discuss this fact below again when we discuss the structural mechanisms and more generally a "state" diagram of polymerization behavior versus λ and ρ_0.

B. Structural properties of the growing chain and the free monomers around the active center

The observed SAW-behavior indicates that for fast growth the chain is spatially self-avoiding, i.e., polymer beads do not overlap. In Fig. 3(a), we compare the average number of overlapping nonbonded chain beads $N_{\rm overlap}(N)$ from the growth simulations with their equilibrium counterparts for θ conditions and good solvent conditions (represented by $\varepsilon = 0.1\,k_BT$). This measure counts the number of overlaps within a threshold distance of $1.5\ \sigma$, and higher counts indicate more collapsed chain topologies. We indeed observe a lower degree of overlap and thus more extended chains for faster reaction conditions. This confirms the observations of Fig. 2 that fast growing chains are more swollen than they would be at equilibrium conditions. The nonequilibrium data for ideal and θ conditions is very well accommodated between

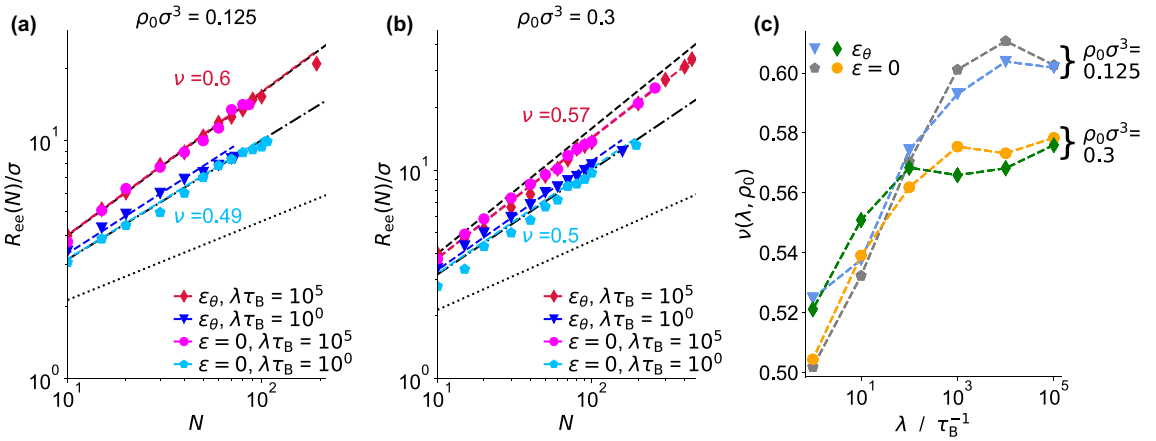

FIG. 2. Scaling behavior of growing polymer chains. [(a) and (b)] End-to-end distances for growing chains $R_{ee}(N)$ in perfectly ideal ($\varepsilon = 0$) and real-chain θ (ε_θ) solvents for slow ($\lambda\tau_B = 1$) and fast ($\lambda\tau_B = 10^5$) rates and for densities $\rho_0 = 0.125$ and 0.3 σ^{-3}, compared with the expected equilibrium behavior for good solvents $\nu = 3/5$ (black dashed), θ solvents $\nu = 1/2$ (black dash-dotted), and poor solvents $\nu = 1/3$ (black dotted). (c) Summary of scaling exponent $\nu(\lambda, \rho_0)$ in dependence of the reaction propensity λ for the two densities and the two solvent qualities as in (a) and (b).

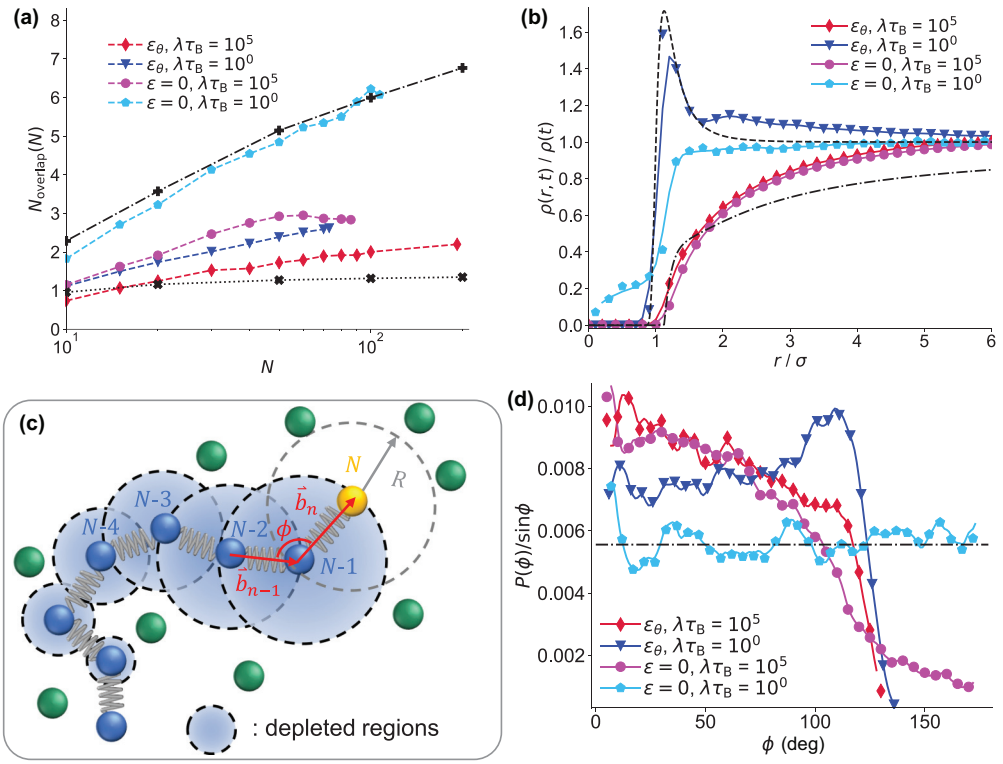

FIG. 3. Structural nonequilibrium properties of growing polymer chains for $\rho_0\sigma^3 = 0.125$. (a) Number of nonbonded chain beads within a distance of 1.5 σ as measure for the overlap $N_{overlap}(N)$. The nonequilibrium results for fast and slow growth are compared with the degree of overlap for equilibrium ideal chains (black, dash-dotted line) and equilibrium chains with essentially repulsive, SAW-like, pairwise interactions of $\varepsilon = 0.1\, k_BT$ (black, dotted line). (b) Normalized radial densities profiles $\rho(r,t)/\rho(t)$ around the active center for different reaction conditions compared with the low-density equilibrium approximation of $g(r)$ for ε_θ (black, dashed line) and the theoretical profile in the steady-state diffusion-controlled ("Smoluchowski") limit $\rho(r,t) = \rho(t)(1 - R/r)$ (black, dash-dotted line). (c) Schematic representation of directed growth of the (yellow) AC of a polymer chain away from the monomer-depleted zones (dashed-line circles) around the reacted blue polymer beads. The green spheres represent free monomers. (d) Probability distribution of bond angles $P(\phi)/\sin\phi$ between the new $\vec{b}_n$ and the previously formed bond vectors $\vec{b}_{n-1}$. The distribution is normalized by $\sin\phi$ to account for the isotropic azimuthal distributions of vectors in 3D space. The black, dash-dotted line represents a homogeneous distribution among all possible angles.

the equilibrium ideal (upper) and equilibrium SAW (lower) bounds in Fig. 3(a).

The self-avoidance can be explained by the nonequilibrium density profiles of free monomers around the ACs $\rho(r,t)/\rho(t)$ plotted in Fig. 3(b): They show a monomer-depleted zone at small distances r even for a completely ideal system at high reaction rates. All monomers in that zone typically react before they approach closer, and thus an excluded volume (nonequilibrium correlation hole) around the active center is created. For the fast reactions, the density profile around the classical Smoluchowski sink with $\rho(r) = 0$ for $r < R$ and $\rho(r)/\rho_\infty = 1 - R/r$ for all $r \geqslant R$ and with $\rho_\infty = \rho(r \to \infty, t)$ as the density of the surrounding bulk liquid serves as a good orientation in the plot. For the slow reactions, no such correlation hole is observed, because the monomers have time to relax between reaction events. The profiles are then near equilibrium, as seen by comparing to the equilibrium radial distribution function in the low-density limit being $\rho(r)/\rho_\infty = g(r) = \exp[-\beta u_{\mathrm{LJ}}(r)]$ for the θ solvent. The presence of interactions leads to an excluded volume around each particle, which manifests at slower reaction in a lower degree of overlap in Fig. 3(a) and $\rho(r,t) = 0$ for $r \lesssim \sigma$ in Fig. 3(b). Only in the ideal case for slow reactions, free monomers are found in very close proximity to the active center ($r < \sigma$), as expected for Doi type of reactions [47].

The depletion and local self-avoidance leads to a directed growth of the polymer chain, which rationalizes the ABP-like behavior and the "persistence factor" α (and persistence time τ_{rot}) introduced in the jump diffusion theory above. The reason, illustrated in Fig. 3(c), is that a newly attached monomer, becoming the AC, has the density depletion hole in the region "behind" it, i.e., at the location of the previous AC. This fact is evidenced by the probability distribution of growth angles $P(\phi)$ in Fig. 3(d): A growth angle, defined by the angle between the previous and the newly formed AC bond as in Fig. 3(c), of $\phi = \pi = 180^\circ$ means that the growth is perfectly "forward," whereas $\phi = 0$ means that the vector points exactly in opposite direction. A flat distribution, i.e., all angles are equally likely and the chain grows randomly, is found in good agreement for the slow, ideal growth of a chain. However, for fast growth, angles larger than $\phi \approx 0.65\pi = 116.5^\circ$ are much more unlikely than for slow growth. This exclusion confirms the concept of depleted zones in the wake of the moving active center.

The observed effect of persistent self-avoiding motion is comparable to a clever worm which eats its way through an apple and which will always move in a direction where there is food, no voids. An ABP analogy has been reported by Merlitz *et al.* [46], where the orientation of the active particles without sensing the concentration gradient is driven by translational or directional memory, leading to pseudochemotaxis [45]. However, in the polymerization case the food (free monomers) can move and diffuse. We actually observe that the depletion holes [cf. Fig. 3(b)] for higher densities become much smaller (see Appendix C) since the percolating pathways and cascadelike reactions (very fast "sprints") are so fast that the monomers do not generate a stationary Smoluchowski density profile. This loss of depletion holes is the structural reason why scaling exponents decrease again for high densities [cf. Fig. 2(d)].

C. Rate and density dependence of the scaling exponents

The nonequilibrium scaling behavior is not limited to ideal or θ conditions. Figure 4(a) shows that the nonequilibrium effect on the scaling exponent $\nu(\varepsilon)$ is observed for all interactions ε, and thus fast growing polymer chains are more extended with respect to their equilibrium counterparts in all solvent conditions (see Appendix B). However, the effect is most substantial in ideal, θ, and poor solvent conditions. As expected, for slow reactions the behavior transits back to the equilibrium situations. For discussing the conditions at which nonequilibrium effects occur more systematically, we screened the growth behavior for the ideal case for various densities ranging from $\rho_0\sigma^3 = 0.01$ to 1.0 and different λ (see Appendix C). The resulting nonequilibrium "state" diagram is depicted in Fig. 4(b), representing random walk, intermediate, and SAW scaling behavior: Slow reactions (low ρ_0 and λ) yield the equilibrium result of $\nu \approx 0.5$ (circles) for θ solvents; increasing ρ_0 and λ causes faster reactions which results in rising values of the scaling exponent closer to a good solvent behavior (squares). For very large densities, roughly beyond the critical Smoluchowski percolation density $\rho \gtrsim \rho_{\mathrm{crit}} \approx 0.43\ \sigma^{-3}$ [see Eq. (5)], the exponents decrease again, as argued above.

IV. CRITERIA FOR TIME-CONTROLLED SOLVENT QUALITY: COMPETITION OF TIMESCALES

To understand the topology of the λ-ρ_0 state diagram theoretically, let us more deeply inspect the timescales in these systems: We have the "process" timescale of reaction, $\tau_{\mathrm{react}} = [\rho k(\lambda, \rho)]^{-1}$, the intrinsic timescales of free monomer diffusion, $\tau_B = \sigma^2/D_0$ (equivalent to b^2/D_0 in our model), and, finally, the timescales of polymer segment relaxation, $\tau_p = b^2/(6\pi^2 D_0)s^2$, for segment size $N/p = s$. As argued before, depletion correlations and persistent directed growth should be visible if the reaction timescale is faster than other relevant relaxation timescales. For Smoluchowski-type depletion holes to be present [recall Fig. 3(b)], the reaction rate should be not slower than the diffusion timescale, i.e., $\tau_{\mathrm{react}} \lesssim \tau_B$. Comparing τ_B and Rouse segment relaxation, τ_p, for this condition, we find that segments of the lengths $s \gtrsim 8$ cannot relax within two reaction events. Hence, we see that if condition $\tau_{\mathrm{react}} \lesssim \tau_B$ is fulfilled, then, according to Rouse, also $\tau_{\mathrm{react}} \lesssim \tau_p$ for a sizable segment length of a minimum of $n = 8$ is satisfied. Hence, very universally a growing segment of a few monomers remains persistent during the (fast) reaction timescale, as indeed observed in our structural analysis.

From these arguments we can estimate a theoretical threshold where nonequilibrium effects should start to play a role: The coloring of the background contours in Fig. 4(b) represents a comparison between the relaxation time $\tau_{\mathrm{relax}} = \tau_{p^*}$ of a Rouse segment with $N/p^* = s^* = 5$ and the reaction scale τ_{react}, using the ratio $\tau_{\mathrm{relax}}/(\tau_{\mathrm{relax}} + \tau_{\mathrm{react}})$. The fit of the segment size of five beads provides the best agreement with the observations from simulations. It is indeed close to the analytical estimate made above. The larger this ratio $\tau_{\mathrm{relax}}/(\tau_{\mathrm{relax}} + \tau_{\mathrm{react}})$ is, e.g., approaching unity, the faster the reaction is compared to the segment relaxation and we observe nonequilibrium behavior. If the ratio is $\ll 1$, then the

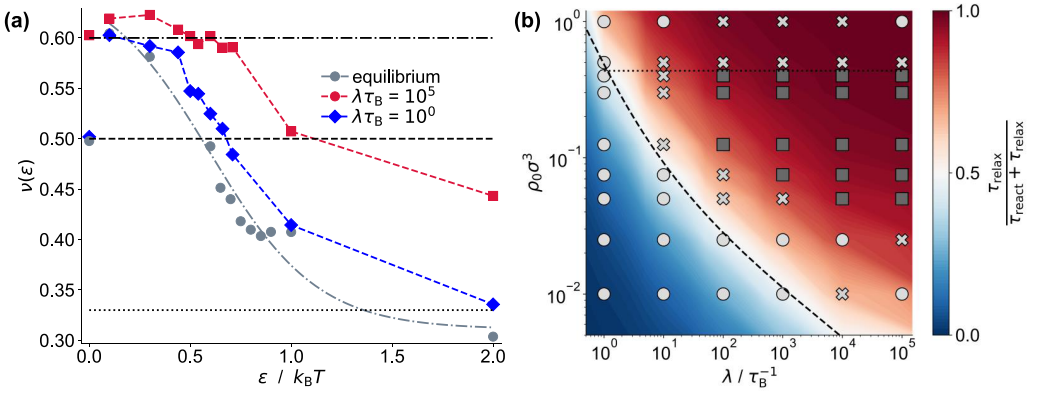

FIG. 4. Summary of conformational scaling and state diagram. (a) Scaling exponent ν as a function of the solvent quality (expressed by interaction paramer ε) for fast growing (red square), slowly growing (blue diamond), and nongrowing polymer chains in equilibrium (gray circle), all at $\rho_0\sigma^3 = 0.125$. The black dash-dotted, dashed, and dotted lines serve as orientation for reference exponents $\nu = 3/5$, $1/2$, and $1/3$, respectively. (b) State diagram for growing ideal polymer chains ($\varepsilon = 0$). The circles, crosses, and squares represent exponents $\nu < 0.525$ (θ solvent), $0.525 \leqslant \nu < 0.55$ (intermediate), and $\nu \geqslant 0.55$ (good solvent), respectively. The smooth contours in the back represent the ratio between reaction timescale τ_{react} and the segmental relaxation τ_{relax} time of a segment with $N/p^* = s^* = 5$. Red regions illustrate chain relaxation times $\tau_{\text{relax}} \gg \tau_{\text{react}}$, while blue regions depict $\tau_{\text{relax}} \ll \tau_{\text{react}}$. The bright-white thin region in between, together with the black dashed line corresponds to the boundary $\tau_{\text{relax}} = \tau_{\text{react}}$. The horizontal black dotted line represents the critical Smoluchowski percolation density $\rho_{\text{crit}} = 0.43\,\sigma^{-3}$, as predicted from the self-consistent Smoluchowski approach, Eq. (5).

segments relax much quicker than new elements are added and the growing chain exhibits equilibrium random walk behavior. The black dashed line in Fig. 4(b), which represents the combinations of λ and ρ_0, where $\tau_{\text{relax}} = \tau_{\text{react}}$, that is, $\tau_{\text{relax}}/(\tau_{\text{relax}} + \tau_{\text{react}}) = 0.5$, represents in good agreement with the simulation data the topology of the boundary between equilibrium and nonequilibrium behavior.

Finally, it is also important to briefly note on another timescale in the problem: the observation (simulation) timescale τ_{sim}, often considered the "Deborah number" in polymer rheology [52]. If this observation window is long and thus the polymer can relax entirely, then also equilibrium scaling of the total chain size should be approached. The simulation timescale can be expressed by the mean number of added monomers N as $\tau_{\text{sim}} = N\tau_{\text{react}}$. Comparing this polymerization time to the polymer segment relaxation of a segment of length s, $N\tau_{\text{react}} = b^2/(6\pi^2 D_0)s^2$ with a fast $\tau_{\text{react}} \lesssim \tau_B = b^2/D_0$ set by the diffusive timescale, we find that segments of size $s \lesssim 8\sqrt{N}$ have maximally relaxed within the time simulated. Hence, for fast reactions, the full chain will never relax in the observation window but only segments with a *relative* amount of the chain decreasing as $\propto 1/\sqrt{N}$. In other words, the longer the polymerization observation, the shorter the relative amount of polymer which has relaxed back to equilibrium. This nonequilibrium relaxation of polymer chains has analogies to the relaxation of chains after releasing them from an applied force f [3,53], only that in the case of polymerization this relaxation will propagate spatially from the beginning (initially polymerized segments) to the growing end, i.e., exhibits strong spatiotemporal heterogeneity.

V. CONCLUDING REMARKS

Our simulations provide molecular-level insight into the nonequilibrium structuring of polymers during chain-growth polymerization in the presence of freely diffusing monomers. In particular, a directed single-chain polymerization appears with increased size scaling exponents at faster reaction conditions. These effects originate from the nonequilibrium density depletion of reacting monomers and the competition of reaction, diffusion and chain relaxation timescales, even in the ideal, fully noninteracting case. Our results complement known concepts of polymerization kinetics for termination rates of many-chain systems, where the chain growth is characterized by "reaction diffusion" jumps and the Trommsdorff-Norrish-effect [17,31,32,40], by novel structural insights. Our insights apply to polymerization on all scales, for example, self-assembly of patchy, colloidal polymers [28,29].

The growth of rather stretched chain morphologies at fast, nonequilibrium conditions compared to collapsed structures in equilibrium at θ or poor solvent conditions might open pathways toward the design and creation of novel adaptive materials [15,16] for industrial applications, potentially using fast 3D and 4D (photo)polymerization techniques [12,26,27]. During nonequilibrium processing, tensely stretched chain segments may contain anisotropic stress and stored energy over their equilibrium counterparts, and controlled storage and delayed energy release back to equilibrium will constitute fascinating aspects for future studies [20,21].

In future studies, our simulation and data analysis framework can also provide insight in the emerging size distributions and nonequilibrium effects of systems containing many growing chains to study the consequences of different processing pathways in more realistic solutions and melts. Experimental evidence of uncontrolled release of stretching energy can be found, for example, in material shrinkage of polymer melts during and after autoacceleration [30]. Furthermore, the experiments conducted by Ramezani *et al.* [54] on the thermodynamic work performed by stressed polymer melts represent a promising direction for future applications of our herein presented simulation framework.

Interestingly, the active centers in fast chain polymerizations behave analogously to ABPs in search of food [45,46], but in contrast to ABPs this originates from the synergistic physics of the growing chain and diffusive monomer motion rather than the properties of the single particles. Due to the analogy, it will be interesting to investigate if polymerization in dense, many-chain systems shows collective behavior similarly rich as for ABPs, such as "swarming," microclustering, ratchet effects, activity-induced phase transitions, or novel interfacial phenomena [44]. Such spatiotemporal pattern formation is very typical in reaction-diffusion processes and, if controllable, can lead to novel hierarchical material structures on various length and timescales.

VI. METHODS

A. Brownian dynamics

We performed all simulations in the LAMMPS software package [55] using the formalism for numerically integrating overdamped Langevin dynamics, that is, Brownian dynamics (BD) simulations. The equation of motion for a particle i is written as

$$\xi_i \dot{\mathbf{r}}_i = -\nabla U(\mathbf{r}_i) + \mathbf{R}(t), \tag{6}$$

where $\dot{\mathbf{r}}_i$ and $\mathbf{r}_i$ denote velocity and position of the ith particle, the drag coefficient ξ_i and the diffusion coefficient D_i are related through the Einstein relation $D_i = k_B T/\xi_i$, and $\mathbf{R}(t)$ is the random force vector. All diffusion coefficients D_i are set to $D_0 = \sigma^2/\tau_B$ with $\sigma = 1.0$ as the van der Waals radius of the particles as well as our unit for length. The components of the random force vector fulfill the properties $\langle R_\alpha(t)\rangle = 0$ and $\langle R_\alpha(t) R_\beta(t')\rangle = 2\xi_i^2 D_i \delta_{\alpha\beta}\delta(t-t')$ with α and β denoting the spatial dimensions and δ being the Dirac δ function. The pairwise nonbonded interactions are described through a 12-6-Lennard-Jones potential, which is written as

$$u_{\mathrm{ij}}^{\mathrm{LJ}}(r_{ij}) = 4\varepsilon\left[\left(\frac{\sigma}{r_{ij}}\right)^{12} - \left(\frac{\sigma}{r_{ij}}\right)^{6}\right], \tag{7}$$

where r_{ij} is the distance between the particles i and j, and ε as the depth of the potential well determines the strength of the interactions as well defines our solvent quality (see Appendix A). Between bonded neighbors i and j in the polymer chain, we only apply a harmonic bond potential with $u_{ij}^{\mathrm{bond}}(b_{ij}) = K_{\mathrm{bond}}(b_{ij} - b_0)^2$, where b_{ij} is magnitude of the bond vector, $K_{\mathrm{bond}} = 20\varepsilon\sigma^{-2}$ is the spring constant, and $b_0 = \sigma$ is the equilibrium bond length. For a free monomer i, the corresponding force acting on it is written as

$$\mathbf{F}_i = -\nabla U(\mathbf{r}_i) = -\sum_{i\neq j}^{N_{m,0}+1} \nabla u_{ij}^{\mathrm{LJ}}(r_{ij}), \tag{8}$$

where $N_{m,0}+1$ is the total number of particles in the system and for the nth (nonterminal) chain bead

$$\mathbf{F}_n = -\nabla u_{n-1,n}^{\mathrm{bond}}(b_{n-1,n}) + \nabla u_{n,n+1}^{\mathrm{bond}}(b_{n,n+1}) - \sum_{j\notin\{n-1,n,n+1\}}^{N_{m,0}+1} \nabla u_{nj}^{\mathrm{LJ}}(r_{nj}), \tag{9}$$

where for the terminal beads $n = 1$ and N, the first or second bonded contribution are omitted, respectively. The positions of all N_{tot} particles are updated using the Euler-Maruyama propagation scheme [56], which is written as

$$\mathbf{r}_i(t+\Delta t) = \mathbf{r}_i(t) + \frac{\Delta t}{\xi_i}\mathbf{F}_i + \sqrt{2D_0\Delta t}\boldsymbol{\zeta}_i, \tag{10}$$

where Δt is the integration time step, which is $10^{-5}\tau_B$ for all systems investigated, and $\boldsymbol{\zeta}_i$ is a vector consisting of random values following a standard normal distribution.

B. Bond formation

Every $(\lambda\Delta t)^{-1}$ integration time steps, the algorithm checks if a bond formation is possible with a probability $p_{\mathrm{react}} = 1.0$. In the simulations, reaction checks are performed between the nearest free monomer and the active center using the cut-off protocol method [35,37,38] following the Doi scheme [47,50,57] using the LAMMPS implementation [38] for creating new bonds within a spherical reactive volume with a reactive radius $R = \sqrt[6]{2}\sigma \approx 1.122\sigma$ around the AC [see Fig. 1(a)]. Once a new bond is formed, the properties of the AC are transferred to the newly added monomer and the previous active center is deactivated.

C. Simulation details

The cubic simulation box with periodic boundary conditions initially contains 1000 nonreacted (free) monomers and a single AC particle as seed for the growing polymer chain. Different number densities $\rho_0 = N_{m,0}/V$ are studied by varying the simulation cell's volume V and keeping the total initial amount of particles $N_{m,0}$ constant. We conducted simulations for observation time windows up to $2\times\ 10^3\,\tau_B$ for densities $\rho_0\sigma^3 = \{0.01,\ 0.025,\ 0.05,\ 0.075,\ 0.125,\ 0.3,\ 0.4,\ 0.5,\ 1.0\}$ for $\varepsilon = 0$. Systems with pairwise interactions of strength $\varepsilon/(k_BT) = \{0.1,\ 0.3,\ 0.44,\ 0.5,\ 0.54,\ 0.6,\ 0.66,\ 0.71,\ 1.0,\ 2.0\}$ have been simulated for the density $\rho_0 = 0.125$. For $\rho_0\sigma^3 = 0.3$, systems with $\varepsilon/(k_BT) = \{0.44,\ 0.54,\ 0.71,\ 0.8,\ 0.9\}$ were studied. All simulations with reaction propensities ranging from slow $\lambda = 10^0$ to fast $\lambda = 10^5\ \tau_B^{-1}$ have been conducted with a self-written wrapper around the LAMMPS software package [55]. The amount of different simulated trajectories for a combination of ε, λ, and ρ_0 ranges from 10^1 to 10^3 independent runs. For comparison with the equilibrium state and for determining a suitable value for ε_θ, simulations of nongrowing polymer chains of lengths $N = \{10,\ 20,\ 50,\ 100,\ 150\}$ have been performed with monomers present at densities $\rho_0\sigma^3 = 0.125$ and 0.3 (see Appendix A).

ACKNOWLEDGMENTS

The authors acknowledge support by the state of Baden-Württemberg through bwHPC and the German Research Foundation (DFG) through Grant No. INST 39/963-1 FUGG (bwForCluster NEMO). The authors thank Benjamin Rotenberg, Stefano Angioletti-Uberti, Sebastian Milster, Matthias Ballauff, and Günter Reiter for inspiring discussions and useful comments.

APPENDIX A: DETERMINATION OF ε_θ FROM CHAINS IN EQUILIBRIUM

This Appendix contains a justification for the choice of the interaction parameter for θ conditions $\varepsilon_\theta/(k_BT) = 0.6$ and 0.8 for densities $\rho_0\sigma^3 = 0.125$ and 0.3, respectively, used throughout our work for the Lennard-Jones pairwise interactions in a BD framework. To represent θ conditions in our simulations, we needed to find a value for ε, where the excluded volume v of the chain beads and the surrounding solvent vanishes with $v = 0$ [5]. It is not sufficient to chose ε such that the second virial coefficient $B_2 = 0$ describing the nature of the pairwise interactions, since a correction considering three-body effects needs to be considered for polymer chains [3,58]. There are many definitions of the θ point [59], but literature reports generally values between $\varepsilon/k_BT = 0.25$ and 0.5 for MD simulations [60], for the Langevin framework [58], and for MC simulations [61–63] in the absence of monomers or cosolvents. It has been reported that chain-length dependent size effects appear, which require an increased value of ε_θ for longer chains N [62–64]. Zhang *et al.* [59] present four different special temperatures in the θ regime, which all differ for noninfinite chain lengths N.

However, except for the work by Heyda *et al.* [58], the influence of explicit solvent molecules in form of cosolutes on the determination of the interactions describing the θ point has not been reported to our knowledge. Therefore, we decided to determine ε_θ for two densities $\rho_0\sigma^3 = 0.125$ and 0.3 from equilibrium simulation without chain growth steps including free monomers as cosolutes. The total amount of particles $N_{\text{tot}} = N + N_m$ with N_m as the amount of monomers remained constant, while the volume was changed to obtain the two different densities. All pairwise interactions between all nonbonded pairs of all species were described by a single radius σ and a single ε.

ε_θ is determined from equilibrium BD simulations of nongrowing polymer chains of lengths $N =$ 10, 20, 50, 100, 150 and a corresponding amount of interacting monomer particles $N_m =$ 990, 980, 950, 900, 850 in the presence of pairwise nonbonded interactions with $\varepsilon/(k_BT) =$ 0.1, 0.3, 0.5, 0.6, 0.65, 0.7, 0.75, 0.8, 0.85, 0.9, 1.0, 2.0. The increasing value of ε corresponds to a decreasing temperature with $\varepsilon \propto T^{-1}$, and larger values of ε lead to more attractive interactions and a globular chain. The smaller ε is, the more extended the chains are. For each combination of N, ρ_0, and ε, up to 30 different trajectories have been simulated and analyzed. Data were collected after equilibrating for at least 5 τ_{Rouse} with the Rouse time $\tau_{\text{Rouse}} \propto N^2$ to ensure a sufficient relaxation of the chain structures. The obtained results for the end-to-end distance R_{ee} and the radius of gyration R_{gyr} are depicted in Figs. 5(a) and 5(c) for densities $\rho_0\sigma^3 = 0.125$ and 0.3, respectively. For determining the universal scaling exponent ν of the polymer size with $R \propto N^\nu$ [1,3–5], both R_{ee} and R_{gyr}, have been fitted [lines in Figs. 5(a) and 5(c)] based on

$$R_{\text{ee}}^2 = b_0^2 N^{2\nu} = 6R_{\text{gyr}}^2, \tag{A1}$$

where b_0 is the equilibrium bond length. Figures 5(b) and 5(d) show the scaling behavior of polymer chains for various ε for $\rho_0\sigma^3 = 0.125$ and 0.3. Interactions of repulsive nature

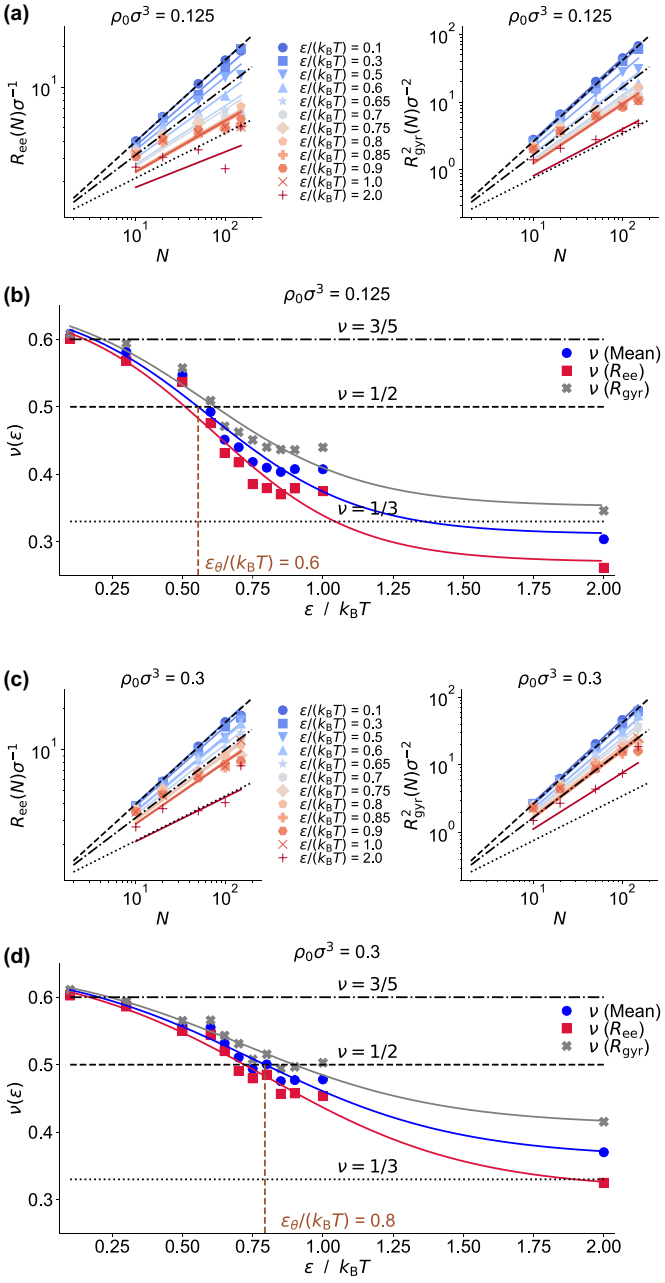

FIG. 5. Determination of the θ point for different ε for different densities ρ_0. Panels (a) and (c) show the mean simulated end-to-end distances $R_{\text{ee}}(N) \propto N^\nu$ and the squared radius gyration $R^2_{\text{gyr}}(N) \propto N^{2\nu}$ for $\rho_0\sigma^3 = 0.125$ and 0.3, respectively. Symbols represent simulation results for a given chain length N and interaction parameter ε. Lines represent the corresponding fits following Eq. (A1), respectively. Dotted, dashed, and dash-dotted line represent theoretical scaling behavior for bad ($\nu = 1/3$), θ ($\nu = 1/2$), and good solvent conditions ($\nu = 3/5$), respectively. Panels (b) and (d) show the ε dependency of the scaling exponent. Circles, squares, and crosses represent fitted scaling exponents $\nu(\varepsilon)$ [Eq. (A1)] from simulated data for R_{ee} (red), R^2_{gyr} (gray), and the mean of the two (blue), respectively. The lines represent the corresponding sigmoidal fits using Eq. (A2). Values for ε_θ are represented by the brown dashed lines. Black dotted, dashed, and dash-dotted line represent theoretical scaling behavior for bad ($\nu = 1/3$), θ ($\nu = 1/2$), and good solvent conditions ($\nu = 3/5$), respectively.

with $\varepsilon/(k_BT) = 0.1 - 0.3$ yield good solvent behavior with $\nu \approx 3/5$ independent of the surrounding monomer concentration. Poor solvent behavior is observed for more attractive values of $\varepsilon/(k_BT) \geqslant 0.7$ for $\rho_0\sigma^3 = 0.125$. At higher densities [$\rho_0\sigma^3 = 0.3$; Fig. 5(d)], free monomers stabilize the more extended chain configurations and therefore higher scaling exponents are found for the same values of ε compared to the lower densities. Only for the lower density, the characteristic bad solvent scaling behavior for higher ε is observed and the chain collapses to a globular state.

All fitted ν_{ee} and ν_{gyr} from Figs. 5(a) and 5(c) are shown together with the mean $\nu_{mean} = 1/2(\nu_{ee} + \nu_{gyr})$ in Figs. 5(b) and 5(d), respectively. The scaling exponents $\nu(\varepsilon)$ are fitted with a sigmoidal fit [lines in Figs. 5(b) and 5(c)] of the form

$$\nu_{fit}(\varepsilon) = A + \frac{B}{C + \exp(-D\varepsilon)}, \tag{A2}$$

where A, B, C, and D represent fitting parameter to interpolate between the simulated data points in good agreement. Solving Eq. (A2) for $\nu_{fit} = 0.5$ then yields $\varepsilon_\theta/(k_BT) \approx 0.6$ and 0.8 for $\rho_0\sigma^3 = 0.125$ and 0.3, respectively. For $\nu(R_{ee})$ at high and low densities, $\varepsilon_\theta/(k_BT) = 0.5$ and 0.7 are obtained, respectively, and for $\nu(R_{gyr})$ 0.6 and $0.9\,k_BT$ are found with respect to the corresponding fits.

Figure 3(a) addresses the degree of overlap with respect to the chain length, and we compared the number of nonbonded neighbors around the chain beads for selected nonequilibrium simulations in comparison with ideal chains and $\varepsilon/(k_BT) = 0.1$. Simulations with this value always yield scaling exponents $\nu \approx 3/5$ representing the good solvent limit.

APPENDIX B: NONEQUILIBRIUM GROWTH BEHAVIOR FOR GOOD AND POOR SOLVENT ε

Figure 4(a) of the article shows that enhanced scaling exponents ν are also found for other values of the interaction strength ε. Especially for $\varepsilon > \varepsilon_\theta$, Fig. 4(a) demonstrates a drastic shift from poor solvent size scaling $\nu \approx 1/3$ and collapsed coils which would be expected for this ε in equilibrium (see Appendix A) to a θ-solvent chain conformation with $\nu \approx 0.5$. Fig. 6 therefore shows selected results from nonequilibrium simulations for $\varepsilon = 0.1\,k_BT$ (good solvent conditions) and $1.0\,k_BT$ (poor solvent conditions). Figures 6(a) and 6(b) show that the more attractive $\varepsilon = 1.0\,k_BT$ leads to a similar diffusion D compared to the more repulsive good solvent counterpart, but the emerging reaction rate constants k are increased in the diffusion-controlled limit. Higher values of ε cause faster reactions due to the more attractive nature.

The size scaling in nonequilibrium for the good solvent case with $\varepsilon = 0.1\,k_BT$ is comparable to the equilibrium as demonstrated by the Figs. 6(c), 6(d), and 6(f). There, the choice of the reaction propensity does not affect the size of the resulting chain structures. However, for poor solvent conditions, a drastic shift toward higher values of ν is observed with an increasing propensity. This manifests in Fig. 6(f), where less compact coil structures appear for fast reactions with $\lambda\tau_B = 10^5$. The higher ν from nonequilibrium chain polymerization in poor solvent conditions compared to their equilibrium equivalents originates from the search for additional monomers and required relaxation time after addition of more monomer to the chain. The density profiles of Fig. 6(e) demonstrate the excluded volume for both values of ε, and also shows the more attractive nature of $\varepsilon = 1.0\,k_BT$, which is pronounced for slow reactions, where free monomers

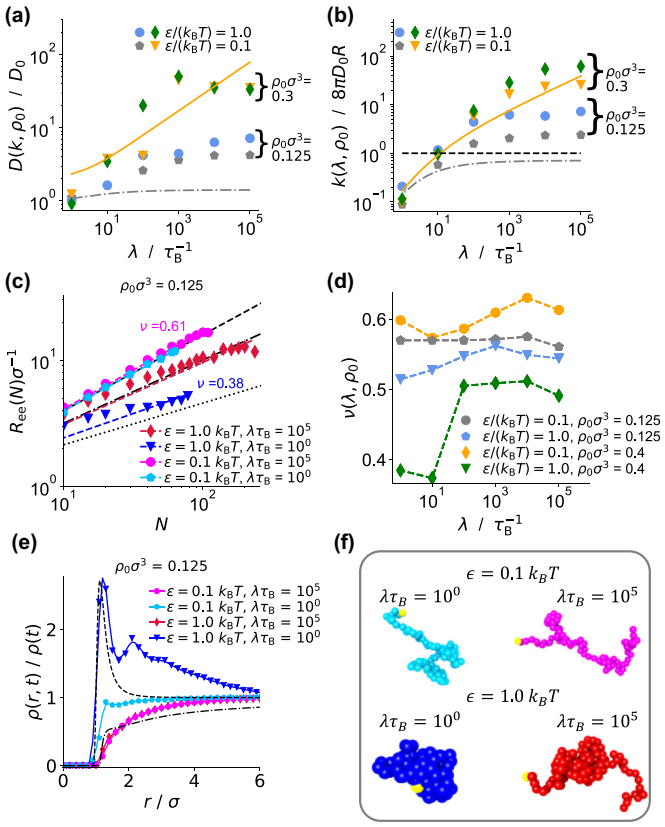

FIG. 6. Growth at good ($\varepsilon = 0.1\,k_BT$) and poor solvent conditions ($\varepsilon = 1.0\,k_BT$) for densities $\rho_0\sigma^3 = 0.125$ and 0.4. (a) Simulated diffusion coefficients D (symbols) for different reaction rates k and initial densities ρ_0. The orange line and the dash-dotted gray line represent the fastest and slowest theoretical limit for $\rho_0\sigma^3 = 0.4$ with $D_{tb} = D_m$ and $\alpha = 1.41$ and for $\rho_0\sigma^3 = 0.125$ with $D_{tb} = D_m/N$ and $\alpha = 1.0$, respectively. (b) Simulated reaction rate constants k (symbols) for different reaction propensities λ and initial densities ρ_0. The orange line and the dash-dotted gray line represents the fastest and slowest theoretical limit for $\rho_0\sigma^3 = 0.4$ with $D_{tb} = D_m$ and $\alpha = 1.41$ and for $\rho_0\sigma^3 = 0.125$ with $D_{tb} = D_m/N$ and $\alpha = 1.0$, respectively, and the dashed black line the fastest Smoluchowksi reaction rate $k_S = 8\pi D_0 R$. (c) End-to-end distance $R_{ee}(N)$ at a density $\rho_0\sigma^3 = 0.125$ for good and poor solvent conditions during fast and slow reactions. Symbols show selected simulated data points, colored dashed lines represent corresponding fits with $R_{ee}(N) \propto N^\nu$. Black dash-dotted, dashed, and dotted lines represent theoretical curves for $\nu = 3/5$ (good solvent), $\nu = 1/2$ (θ solvent), and $\nu = 1/3$ (poor solvent). (d) Size scaling exponents ν for different propensities λ. (e) Normalized densities profiles $\rho(r,t)/\rho(t)$ around the active site for different reaction conditions compared with the theoretical profile in the diffusion-controlled ("Smoluchowski") limit $\rho(r,t) = \rho(t)(1 - R/r)$ (black, dash-dotted line) [47,65] and the low-density equilibrium approximation $g(r)$ for $\varepsilon_\theta/(k_BT) = 1.0$ (black, dashed line). (f) snapshots of chains at different solvent conditions for a density $\rho_0\sigma^3 = 0.125$ at fast ($\lambda\tau_B = 10^5$) and slow ($\lambda\tau_B = 10^0$) reaction conditions with yellow-colored active sites.

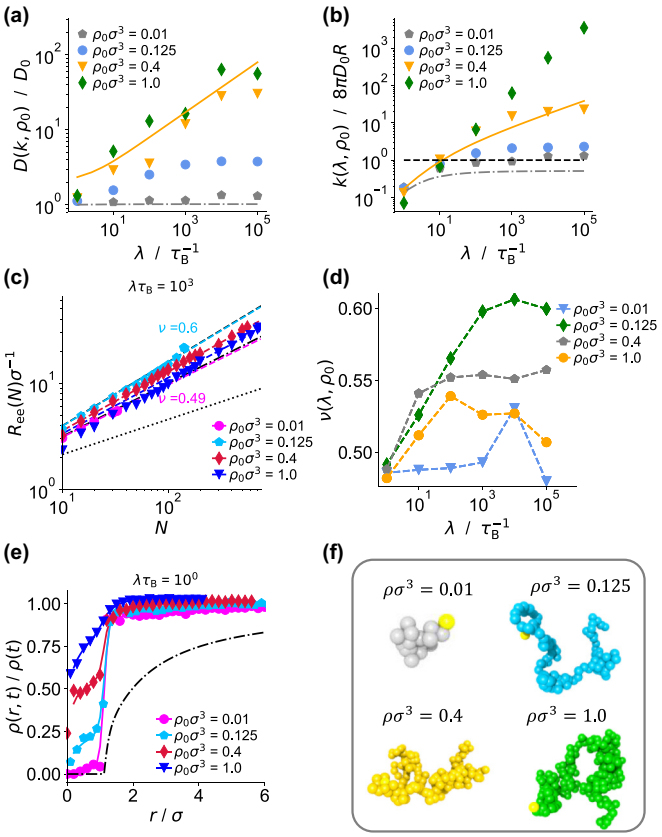

FIG. 7. Growth in an ideal solvent at different initial densities. (a) Diffusion coefficients D (symbols) for different reaction rates k and initial densities ρ_0. The orange line and the dash-dotted gray line represent the fastest and slowest theoretical limit for $\rho_0\sigma^3 = 1.0$ with $D_{\rm tb} = D_m$ and $\alpha = 1.41$ and for $\rho_0\sigma^3 = 0.01$ with $D_{\rm tb} = D_m/N$ and $\alpha = 1.0$, respectively. (b) Simulated reaction rate constants k (symbols) for different reaction propensities λ and initial densities ρ_0. The orange line and the dash-dotted gray line represents the fastest and slowest theoretical limit for $\rho_0\sigma^3 = 1.0$ with $D_{\rm tb} = D_m$ and $\alpha = 1.41$ and for $\rho_0\sigma^3 = 0.01$ with $D_{\rm tb} = D_m/N$ and $\alpha = 1.0$, respectively, and the dashed black line the fastest Smoluchowksi reaction rate $k_S = 8\pi D_0 R$. (c) End-to-end distance at different densities for an intermediate reaction frequency $\lambda\tau_B = 10^3$. Symbols show selected simulated data points, colored dashed lines represent corresponding fits with $R_{\rm ee}(N) \propto N^{\nu}$. Black dash-dotted, dashed, and dotted lines represent theoretical curves for $\nu = 3/5$ (good solvent), $\nu = 1/2$ (θ solvent), and $\nu = 1/3$ (poor solvent). (d) Size scaling exponents ν for different propensities λ. (e) Normalized densities profiles $\rho(r,t)/\rho(t)$ around the active site for different reaction conditions compared with the theoretical profile in the diffusion-controlled ("Smoluchowski") limit $\rho(r,t) = \rho(t)(1 - R/r)$ (black, dash-dotted line) [47,65]. (f) Snapshots of fast growing chains ($\lambda\tau_B = 10^5$) with yellow-colored active sites.

accumulate around the active site between two reaction events. In the case of fast reactions, the two different solvent conditions lead to similar density profiles relatively close to the Smoluchowski limit for ideal, diffusion-controlled reactions.

APPENDIX C: DENSITY EFFECTS ON GROWING CHAIN FOR IDEAL SOLVENTS

Figure 4(b) contains simulated data points describing the scaling behavior for initial densities ranging from $\rho_0\sigma^3 = 0.01$ to 1.0. Both the lower and upper simulated limit for the density show reduced scaling exponents ν for the different reaction propensities λ. For a low density $\rho_0\sigma^3 = 0.01$, this is not surprising, since the number of reactions events and jumps is low and reactions kinetics in the fast limit are comparable to the Smoluchowski rate constant for bimolecular reactions of two moving particles Figs. 7(a) and 7(b). The simulated data points are found close to our suggested theoretical slow limit (gray, dash-dotted line) based on Eq. (4) for $D_{\rm tb} \simeq D_m/N$. High densities $\rho_0\sigma^3 = 0.4$ and 1.0 lead to fast reactions, and since the later one is above the critical percolation density $\rho_{\rm crit}\sigma^3 \approx 0.43$ [Eq. (5)], extremely high reaction rates k are reported, which are only limited by the propensity λ and the technical constraint of allowing only two bond formations per reaction time step. It should be noted that only $\rho_0\sigma^3 = 0.4$ is more or less still covered by theoretical data (orange line) using Eq. (4) with $D_{\rm tb} \simeq D_m$, but no meaningful theory is accessible beyond $\rho_{\rm crit}$ due to divergence of the numerical solutions.

Figures 7(c), 7(d), and 7(f) demonstrate the different size scaling $R_{\rm ee} \propto N^{\nu}$ behavior dependent on the density. Low densities of $\rho_0\sigma^3 = 0.01$ and thus slow reactions allow a relaxation of chains between reaction events and structures with $\nu \approx 1/2$ representing θ conditions for all reaction propensities λ studied are obtained. As shown in the article, densities between $\rho_0\sigma^3 = 0.125$ and 0.3 lead to enhanced scaling exponents close to the good solvent limit $\nu \approx 3/5$. Higher densities $\rho_0\sigma^3 > 0.3$ do not lead to a further increase of ν, but rather show again a decreasing tendency back toward random walk and θ-solvent behavior with increasing density.

We explain this nonmonotonic behavior of the scaling exponent ν for an increasing density with an increased number of monomers in each reactive volume around an active site [Fig. 7(e)] and the increased reaction rate [Fig. 7(b)]. At high densities close to and above the critical density $\rho_{\rm crit}\sigma^3 \approx 0.43$, potentially monomer-depleted zones are filled up quickly and orientation memory $\tau_{\rm rot}$ represented by a few chain elements is negligible with respect to the growth rate. Form a macroscopic perspective, the chain growth performs a random walk through the dense monomer melt. The enhanced size scaling exponent is only observed for densities below a critical percolation threshold $\rho_{\rm crit}$.

[1] P. J. Flory, *Principles of Polymer Chemistry* (Cornell University Press, Ithaca, NY, 1953).
[2] I. M. Lifshitz, A. Y. Grosberg, and A. R. Khokhlov, Rev. Mod. Phys. **50**, 683 (1978).
[3] P.-G. de Gennes, *Scaling Concepts in Polymer Physics* (Cornell University Press, Ithaca, NY, 1979).
[4] M. Doi and S. F. Edwards, *The Theory of Polymer Dynamics* (Oxford University Press, Oxford, 1986).

[5] M. Rubinstein and R. H. Colby, *Polymer Physics* (Oxford University Press, Oxford, 2003).

[6] H. S. Chan and K. A. Dill, Proc. Natl. Acad. Sci. USA **87**, 6388 (1990).

[7] J. N. Onuchic, Z. Luthey-Schulten, and P. G. Wolynes, Annu. Rev. Phys. Chem. **48**, 545 (1997).

[8] V. S. Pande, A. Y. Grosberg, and T. Tanaka, Rev. Mod. Phys. **72**, 259 (2000).

[9] M. Ballauff and C. N. Likos, Angew. Chemie Int. Ed. **43**, 2998 (2004).

[10] H. Hofmann, A. Soranno, A. Borgia, K. Gast, D. Nettels, and B. Schuler, Proc. Natl. Acad. Sci. U.S.A. **109**, 16155 (2012).

[11] C. P. Brangwynne, P. Tompa, and R. V. Pappu, Nat. Phys. **11**, 899 (2015).

[12] S. C. Ligon, R. Liska, J. Stampfl, M. Gurr, and R. Mülhaupt, Chem. Rev. **117**, 10212 (2017).

[13] M. A. C. Stuart, W. T. S. Huck, J. Genzer, M. Müller, C. Ober, M. Stamm, G. B. Sukhorukov, I. Szleifer, V. V. Tsukruk, M. Urban, F. Winnik, S. Zauscher, I. Luzinov, and S. Minko, Nat. Mater. **9**, 101 (2010).

[14] K. R. Thomas, A. Chenneviere, G. Reiter, and U. Steiner, Phys. Rev. E **83**, 021804 (2011).

[15] X. Liu, H. Yuk, S. Lin, G. A. Parada, T.-C. Tang, E. Tham, C. de la Fuente-Nunez, T. K. Lu, and X. Zhao, Adv. Mater. **30**, 1704821 (2018).

[16] A. Walther, Adv. Mater. **32**, 1905111 (2020).

[17] P.-G. de Gennes, J. Chem. Phys. **76**, 3316 (1982).

[18] N. M. Toan, G. Morrison, C. Hyeon, and D. Thirumalai, J. Phys. Chem. B **112**, 6094 (2008).

[19] A. Alexander-Katz, H. Wada, and R. R. Netz, Phys. Rev. Lett. **103**, 028102 (2009).

[20] S. Chandran, J. Baschnagel, D. Cangialosi, K. Fukao, E. Glynos, L. M. C. Janssen, M. Müller, M. Muthukumar, U. Steiner, J. Xu, S. Napolitano, and G. Reiter, Macromolecules **52**, 7146 (2019).

[21] G. Reiter, J. Chem. Phys. **152**, 150901 (2020).

[22] T. Guérin, O. Bénichou, and R. Voituriez, Nat. Chem. **4**, 568 (2012).

[23] H. H. Katkar and M. Muthukumar, J. Chem. Phys. **148**, 024903 (2018).

[24] I. Chubak, C. N. Likos, K. Kremer, and J. Smrek, Phys. Rev. Res. **2**, 043249 (2020).

[25] S. Penczek and G. Moad, Pure Appl. Chem. **80**, 2163 (2008).

[26] A. Bagheri and J. Jin, ACS Appl. Polym. Mater. **1**, 593 (2019).

[27] S. Telitel, J. C. Morris, Y. Guillaneuf, J.-L. Clément, F. Morlet-Savary, A. Spangenberg, J.-P. Malval, J. Lalevée, D. Gigmes, and O. Soppera, ACS Appl. Mater. Interfaces **12**, 30779 (2020).

[28] F. Sciortino, E. Bianchi, J. F. Douglas, and P. Tartaglia, J. Chem. Phys. **126**, 194903 (2007).

[29] A. H. Gröschel, A. Walther, T. I. Löbling, F. H. Schacher, H. Schmalz, and A. H. E. Müller, Nature (Lond.) **503**, 247 (2013).

[30] Q. Tran-Cong-Miyata and H. Nakanishi, Polym. Int. **66**, 213 (2017).

[31] G. V. Schulz, Z. Phys. Chem. **8**, 290 (1956).

[32] D. S. Achilias and C. Kiparissides, Macromolecules **25**, 3739 (1992).

[33] C. Liu, K. Kubo, E. Wang, K.-S. Han, F. Yang, G. Chen, F. A. Escobedo, G. W. Coates, and P. Chen, Science **358**, 352 (2017).

[34] R. Dockhorn, L. Plüschke, M. Geisler, J. Zessin, P. Lindner, R. Mundil, J. Merna, J.-U. Sommer, and A. Lederer, J. Am. Chem. Soc. **141**, 15586 (2019).

[35] R. L. C. Akkermans, S. Toxværd, and W. J. Briels, J. Chem. Phys. **109**, 2929 (1998).

[36] M. Perez, O. Lame, F. Leonforte, and J.-L. Barrat, J. Chem. Phys. **128**, 234904 (2008).

[37] K. Farah, F. Müller-Plathe, and M. C. Böhm, ChemPhysChem **13**, 1127 (2012).

[38] P. de Buyl and E. Nies, J. Chem. Phys. **142**, 134102 (2015).

[39] H. Liu, Y.-L. Zhu, Z.-Y. Lu, and F. Müller-Plathe, J. Comput. Chem. **37**, 2634 (2016).

[40] G. T. Russell, D. H. Napper, and R. G. Gilbert, Macromolecules **21**, 2133 (1988).

[41] J. W. Lyklema and K. Kremer, J. Phys. A. Math. Gen. **17**, L691 (1984).

[42] A. S. Padmanabhan and S. Jacob, J. Math. Chem. **52**, 627 (2014).

[43] A. Taniya, M. Deepthi, and A. Padmanabhan, AIP Adv. **8**, 065205 (2018).

[44] C. Bechinger, R. Di Leonardo, H. Löwen, C. Reichhardt, G. Volpe, and G. Volpe, Rev. Mod. Phys. **88**, 045006 (2016).

[45] I. Richard Lapidus, J. Theor. Biol. **86**, 91 (1980).

[46] H. Merlitz, H. D. Vuijk, R. Wittmann, A. Sharma, and J.-U. Sommer, PLoS One **15**, e0230873 (2020).

[47] M. Dibak, C. Fröhner, F. Noé, and F. Höfling, J. Chem. Phys. **151**, 164105 (2019).

[48] P. W. Atkins and J. de Paula, *Physical Chemistry*, 9th ed. (W. H. Freeman and Company, New York, 2010).

[49] K. S. Anseth, C. M. Wang, and C. N. Bowman, Macromolecules **27**, 650 (1994).

[50] M. Doi, Chem. Phys. **11**, 107 (1975).

[51] P. E. Rouse, J. Chem. Phys. **21**, 1272 (1953).

[52] M. Reiner, Phys. Today **17**, 62 (1964).

[53] Y.-J. Sheng, P.-Y. Lai, and H.-K. Tsao, Phys. Rev. E **56**, 1900 (1997).

[54] F. Ramezani, J. Baschnagel, and G. Reiter, Phys. Rev. Mater. **4**, 082601(R) (2020).

[55] S. Plimpton, J. Comput. Phys. **117**, 1 (1995).

[56] D. L. Ermak and J. A. McCammon, J. Chem. Phys. **69**, 1352 (1978).

[57] R. Erban and S. J. Chapman, Phys. Biol. **6**, 046001 (2009).

[58] J. Heyda, A. Muzdalo, and J. Dzubiella, Macromolecules **46**, 1231 (2013).

[59] P. Zhang, N. M. Alsaifi, and Z.-G. Wang, Macromolecules **53**, 10409 (2020).

[60] M. Cieśla, J. Pawlowicz, and L. Longa, Acta Phys. Pol. B **38**, 1727 (2007).

[61] A. M. Rubio, J. J. Freire, J. H. R. Clarke, C. W. Yong, and M. Bishop, J. Chem. Phys. **102**, 2277 (1995).

[62] C. W. Yong, J. H. R. Clarke, J. J. Freire, and M. Bishop, J. Chem. Phys. **105**, 9666 (1996).

[63] W. W. Graessley, R. C. Hayward, and G. S. Grest, Macromolecules **32**, 3510 (1999).

[64] A. Milchev, W. Paul, and K. Binder, J. Chem. Phys. **99**, 4786 (1993).

[65] M. von Smoluchowski, Z. Phys. Chem. **92U**, 129 (1918).